Cooperative dynamics of DNA-grafted magnetic nanoparticles optimize magnetic biosensing and coupling to DNA origami

Aidin Lak, Yihao Wang, Pauline J. Kolbeck, Christoph Pauer, Mohammad Suman Chowdhury, Marco Cassani, Frank Ludwig, Thilo Viereck, Florian Selbach, Philip Tinnefeld, Meinhard Schilling, Tim Liedl, Joe Tavacoli, Jan Lipfert

Angaben zur Veröffentlichung / Publication details:

Lak, Aidin, Yihao Wang, Pauline J. Kolbeck, Christoph Pauer, Mohammad Suman Chowdhury, Marco Cassani, Frank Ludwig, et al. 2024. "Cooperative dynamics of DNA-grafted magnetic nanoparticles optimize magnetic biosensing and coupling to DNA origami." Nanoscale 16 (15): 7678–89. https://doi.org/10.1039/d3nr06253h.

Nanoscale

ROYAL SOCIETY OF CHEMISTRY

PAPER

View Article Online
View Journal | View Issue

Cite this: *Nanoscale*, 2024, **16**, 7678

Cooperative dynamics of DNA-grafted magnetic nanoparticles optimize magnetic biosensing and coupling to DNA origami†

Aidin Lak, *[a] Yihao Wang,[a] Pauline J. Kolbeck,[b,c] Christoph Pauer,[b] Mohammad Suman Chowdhury,[a] Marco Cassani,[d] Frank Ludwig,[a] Thilo Viereck,[a] Florian Selbach,[e] Philip Tinnefeld,[e] Meinhard Schilling,[a] Tim Liedl,[b] Joe Tavacoli[b] and Jan Lipfert[b,c]

Magnetic nanoparticles (MNPs) provide new opportunities for enzyme-free biosensing of nucleic acid biomarkers and magnetic actuation by patterning on DNA origami, yet how the DNA grafting density affects their dynamics and accessibility remains poorly understood. Here, we performed surface functionalization of MNPs with single-stranded DNA (ssDNA) *via* click chemistry with a tunable grafting density, which enables the encapsulation of single MNPs inside a functional polymeric layer. We used several complementary methods to show that particle translational and rotational dynamics exhibit a sigmoidal dependence on the ssDNA grafting density. At low densities, ssDNA strands adopt a coiled conformation that results in minor alterations to particle dynamics, while at high densities, they organize into polymer brushes that collectively influence particle dynamics. Intermediate ssDNA densities, where the dynamics are most sensitive to changes, show the highest magnetic biosensing sensitivity for the detection of target nucleic acids. Finally, we demonstrate that MNPs with high ssDNA grafting densities are required to efficiently couple to DNA origami. Our results establish ssDNA grafting density as a critical parameter for the functionalization of MNPs for magnetic biosensing and functionalization of DNA nanostructures.

Received 7th December 2023,
Accepted 9th March 2024

DOI: 10.1039/d3nr06253h

rsc.li/nanoscale

Introduction

DNA-grafted inorganic nanoparticles (NPs) are versatile building blocks for superstructures of selected geometries and functionalities as well as responsive nanomaterials for biosensing and biocomputing.[1–5] DNA-labelled NPs and nanostructures have been used as molecular nanothermometers,[6] *in vitro* biosensors,[7] and nanoparticle beacons[8] and for intracellular sensing and molecular recognition.[9,10] NP–DNA conjugates offer novel possibilities for further modifications through competitive hybridization,[11] DNA strand displacement,[7] and ligation.[12] The functionalization of Au NPs with ssDNA can be achieved through direct Au–S covalent bonds, making it straightforward and requiring only minimal surface modification steps. Consequently, Au NP–DNA conjugates have been combined with DNA origami nanotechnology to develop novel tools and applications, for example chiral plasmonic nanostructures, plasmonic rulers, and nanoantennas for biosensing.[13–20]

Colloidal magnetic nanoparticles (MNPs) transduce magnetic energy to heat under alternating magnetic fields, a feature that is harnessed in magnetic hyperthermia-triggered drug delivery and magnetic actuation of cellular processes.[21–23] Combining the potential for local heating by external fields with the well-defined melting temperature of double-stranded DNA (dsDNA) has led to molecular magnetic nanothermometers.[6] Furthermore, MNPs can change their Brownian magnetic relaxation dynamics by binding to targeting molecules,[24,25] upon which magnetic biosensing has been

[a]*Institute for Electrical Measurement Science and Fundamental Electrical Engineering and Laboratory for Emerging Nanometrology (LENA), Hans-Sommer-Str. 66, Braunschweig, 38106, Germany. E-mail: a.lak@tu-braunschweig.de*
[b]*Soft Condensed Matter and Biophysics, Department of Physics and Debye Institute for Nanomaterials Science, Utrecht University, Princetonplein 1, 3584 CC Utrecht, The Netherlands*
[c]*Department of Physics and Debye Institute for Nanomaterials Science, Utrecht University, Princetonplein 1, 3584 CC Utrecht, The Netherlands*
[d]*International Clinical Research Center, St. Anne's University Hospital, Brno, Czech Republic*
[e]*Department of Chemistry and Center for NanoScience, LMU Munich, 81377 Munich, Germany*

†Electronic supplementary information (ESI) available: Synthesis protocols, characterization techniques, analysis routines, and supplementary Fig. S1–S8. See DOI: https://doi.org/10.1039/d3nr06253h

built for the detection of bacteria,[26] proteins,[27,28] and DNA/RNA.[29–31] Magnetic-based assays offer an enzyme-, wash-, and amplification-free[7] detection workflow, which are highly desirable features for point-of-care detection of nucleic acid biomarkers. A particular challenge stems from the multistep premodification and surface chemistries that are needed for successful DNA labeling of MNPs.[32] In contrast to Au NPs, an intermediate encapsulation layer with a well-defined chemistry, functionality, and organization is required to bind ssDNA to MNPs.[33] Surface silanization is commonly used to premodify the particle surface.[34,35] Electrostatic interactions between charged nanoparticles and dsDNA macromolecules have been successfully used to attach DNA to MNPs, yet only after a multistep surface silanization.[36,37] However, the accessibility and targeting ability of ssDNA bound *via* unspecific charge interactions are rather poor due to the binding of DNA to multiple positive head groups, causing them to flatten on the particle surface. Amine-modified ssDNA strands have been covalently conjugated to MNPs,[38,39] again after surface silanization.[40,41] High affinity streptavidin–biotin interactions have also been used to label MNPs with ssDNA.[42,43] Encapsulation of iron oxide NPs in an amphiphilic polymer that enables copper-free click chemistry conjugation has enabled their assembly into superlattices[44] and binding to DNA origami structures.[45] Most previous studies have addressed DNA labeling of magnetic microbeads for DNA purification and cell sorting.[46,47] However, particles for Brownian relaxation-based magnetic assays are typically much smaller, with sizes < 50 nm.[48,49] These particles, often referred to as single-core MNPs, offer a high binding capacity for the target, yet their controlled and reliable bio-labeling is largely unexplored. Therefore, our understanding about how the DNA grafting density influences the particle dynamics, their reactivity toward complementary sequences, and thus their suitability for magnetic assays and patterning on DNA origami is still limited.

Here we demonstrate clickable magnetic nanoparticles (CMPs) enabling copper-free click chemistry conjugation as a highly versatile nanoplatform to tune the grafting density of ssDNA over a broad range. We show that magnetic relaxation, hydrodynamics, and electrophoretic dynamics of CMP–DNA conjugates change in a cooperative manner in response to ssDNA grafting, which can be described by the Hill equation. Whereas at a low grafting density, the ssDNA strands are coiled on CMPs and minimally influence the dynamics of CMPs, at a high grafting density they form dense polymer brushes and cooperatively change the dynamics of CMPs. Exploiting our CMPs as nanomarkers for magnetic-based biosensing, we found that CMP–DNA conjugates at the ssDNA grafting density corresponding to the midpoint of the Hill equation exhibit the largest change in the magnetic signal upon hybridization with the target sequence. We propose that the ssDNA strands are in a mixture of coiled and brushed states at the intermediate grafting density. This configuration leads to the largest change in the magnetic relaxation dynamics of particles upon duplexing with the target nucleic acids. In addition, we demonstrate the coupling of our CMP–DNA conjugates to six-(6 HB) and 24-helix-bundle (24 HB) DNA origami structures. We found that a high ssDNA grafting density favors binding to DNA origami structures with high efficiency and site specificity.

Results and discussion

Polymer encapsulation of magnetic nanoparticles provides high colloidal stability and enables copper-free click chemistry conjugation

To investigate the effects of ssDNA grafting density on particle dynamics and their accessibility toward target DNA strands with magnetic techniques, we used MNPs relaxing *via* a Brownian relaxation mechanism. We, therefore, synthesized cubic-shape cobalt-doped iron oxide MNPs using a high temperature decomposition synthesis procedure (see the ESI† for details).[49] The stoichiometry was determined to be $Co_{0.85}Fe_{2.15}O_4$ by inductively-coupled plasma optical emission spectroscopy (ICP-OES) and the mean particle side length L_c to be 15.8 ± 1.2 nm (mean ± standard deviation) by transmission electron microscopy (TEM; Fig. 1a and c).

The MNPs were transferred to the aqueous phase by applying the "grafting to" polymer coating approach using poly (maleic anhydride-*alt*-1-octadecene) (PMAO) copolymers by adopting the procedure reported by Pellegrino *et al.*[50] To obtain singly-coated and "clickable" MNPs (CMPs), we first modified PMAO copolymers with polyethylene glycol (PEG)(3)-azide linkers and further optimized the original polymer coating procedure (see the ESI† for details). The conjugation of NH_2-PEG(3)-azide linkers to PMAO was carried out through an anhydride ring opening reaction in dimethylformamide.[51] During the polymer coating procedure and by gradual removal of chloroform, the C16 carbon chains of PMAO interact hydrophobically with the C18 chains of oleic acid and form a dense shell around the MNPs. To visualize the polymeric shell and examine its uniformity and morphology, we performed negative-stain TEM imaging (Fig. 1b). We observed that MNPs are uniformly coated with a ~3 nm layer of the PMAO–PEG polymer. Moreover, most CMPs are singly enveloped inside the polymeric shell after the coating process. An interesting observation is that the PMAO–PEG copolymer shell around MNPs follows the cubic shape of particles (Fig. 1b). Atomic force microscopy (AFM) images of CMPs deposited on a mica substrate by adding Na^+ to particle suspensions show that the CMPs are monodisperse and sparsely distributed on the substrate (Fig. S1†). From the analysis of AFM images, we found that the particle height H increases from L_c = 15.8 ± 1.2 nm (from TEM) to H = 24.0 ± 2.6 nm (mean ± standard deviation (std)) after polymer coating (Fig. 1c). Considering 1.8 nm and ~1 nm for the length of a C18 chain of oleic acid and a PEG linker with 3 units, respectively,[52] we expect an increase in size after the polymer coating by 2 × 1.8 nm + 2 × 1 nm = 5.6 nm, in good agreement with the experimentally observed difference between H and an L_c of 8.2 ± 3.8 nm. Dynamic light scattering

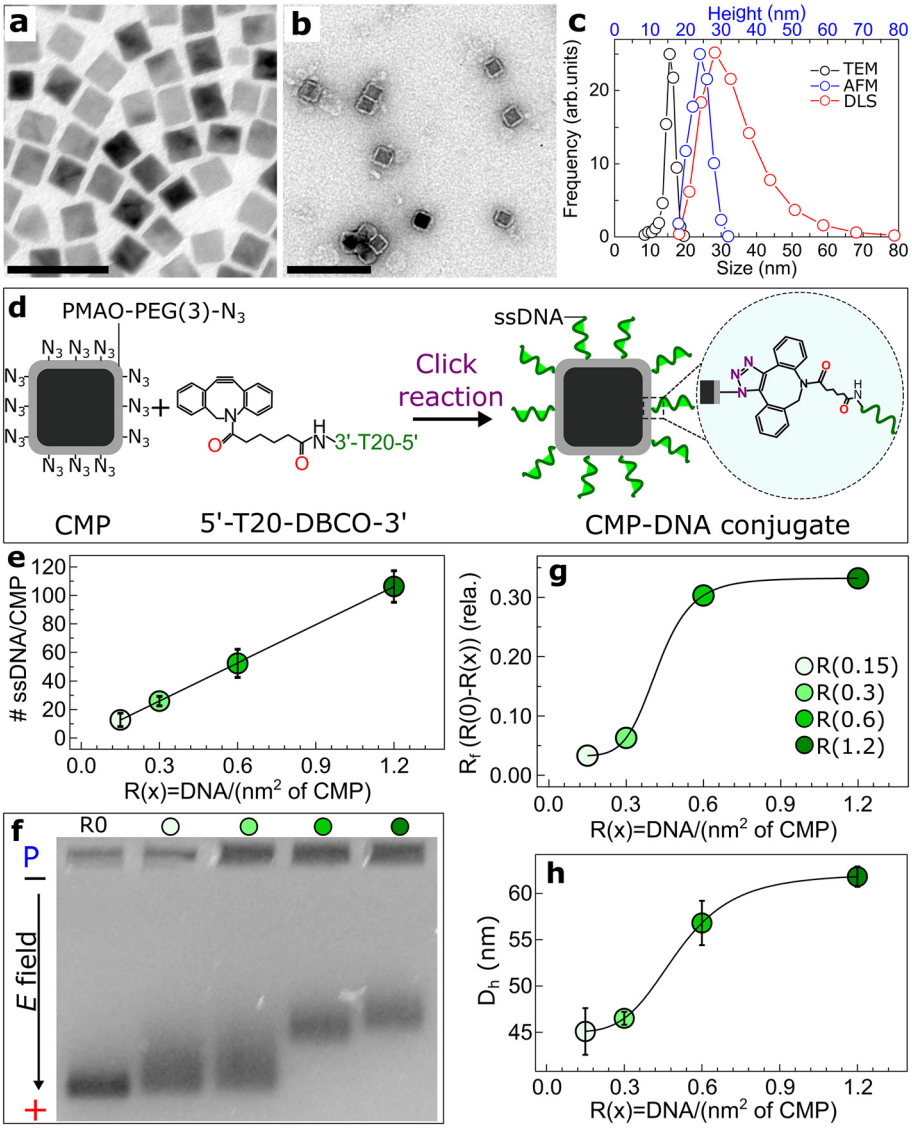

Fig. 1 Functionalization and characterization of oleic acid-coated MNPs, CMPs, and CMP–DNA conjugates. (a) Typical transmission electron microscopy (TEM) micrograph of the initial oleic acid-coated MNPs in chloroform. (b) Negative-stain (1% uranyl formate) TEM micrograph of MNPs after PMAO–PEG(3)-azide coating (CMPs), but before ssDNA labeling. The scale bars are 50 and 100 nm in panels (a) and (b), respectively. (c) Side length L_c of oleic acid-coated MNPs (from panel (a)) and the height H (AFM) and hydrodynamic diameter D_h of CMPs after polymer coating. The height histogram was acquired from the analysis of AFM micrographs (Fig. S1†). The D_h distribution was recorded using a Malvern Zetasizer Nano instrument on CMPs dispersed in Tris-EDTA (TE) buffer (5 mM Tris, 1 mM EDTA, 5 mM NaCl, pH 7.3). (d) Scheme of the strain-promoted azide–alkyne cycloaddition (SPAAC) copper-free click reaction between azide-labelled CMPs and dibenzocyclooctyne (DBCO)-modified ssDNA oligomers. (e) Average number of ssDNA per CMP ± standard error of the mean (SEM) as estimated from the depletion assays *vs.* the nominal grafting density $R(x)$. (f) Agarose gel electrophoresis shift assays performed on CMPs and CMP–DNA conjugates at different $R(x)$ values on a 0.5% agarose gel, P stands for loading pockets. (g) Relative position of the gel front (R_f) of CMP–DNA conjugates relative to the $R(0)$ sample with no ssDNA as a function of $R(x)$. (h) Volume-weighted particle hydrodynamic size (D_h) of CMP–DNA conjugates ± SEM as a function of $R(x)$. Solid lines in panels (g) and (h) are fits of the Hill equation with fitted parameters R_{half} = 0.42 DNA nm^{-2} and n = 6.3 and R_{half} = 0.48 DNA nm^{-2} and n = 4.5, respectively.

(DLS) reveals that the CMPs are colloidally stable with no detectable aggregates (Fig. 1c). The number-weighted particle hydrodynamic diameter D_h is 32.3 ± 8.8 nm with a polydispersity index (PDI) of 0.1. The ~8 nm difference between D_h and H is likely due to hydration, an electrical double layer that is formed around the charged CMPs in solution, and the fact that D_h is the effective diameter of an equivalent sphere.

The number of ssDNA per nanoparticle increases linearly with nominal grafting density

Our single-core CMPs offer an excellent nanoplatform to tune the grafting density of ssDNA to study its effect on the dynamic properties of the particles. We used the strain-promoted azide–alkyne cycloaddition (SPAAC) copper-free click

chemistry to efficiently graft dibenzocyclooctyne (DBCO)-modified ssDNA strands of 20-mer thymine $(T)_{20}$ on CMPs (Fig. 1d). We designed our DNA labeling experiments using the grafting density parameter $R(x)$, defined by the nominal number of ssDNA per nm^2 of CMPs, using the concentrations of CMPs and ssDNA in the reaction mixture and assuming the particle surface area to be $6 \cdot \left(D_h/\sqrt{3}\right)^2$ (see the discussion in the ESI†). We note that using the height determined from AFM to compute the surface area would only linearly rescale the nominal $R(x)$ by a small factor. Accordingly, we synthesized CMP–DNA conjugates at four different $R(x)$ values of 0.15, 0.3, 0.6, and 1.2 ssDNA per nm^2 of CMPs. To determine the actual number of ssDNA per CMP at each nominal $R(x)$, we performed depletion assays by measuring UV absorption spectra of the supernatants of freshly DNA-labelled CMPs after centrifugation and particle pelleting. Three sequential supernatants after particle re-dispersion and centrifugation were measured, as exemplarily shown for the case of $R(x) = 0.3$ (Fig. S2†). We converted the absorption at 260 nm to the number of ssDNA strands using the Beer–Lambert equation after correcting for background from particles (see the ESI for protocols and equations and Fig. S2†). Remarkably, we found that the average number of ssDNA strands per CMP increases linearly with the nominal density $R(x)$ (Fig. 1e and Fig. S2†). Our data suggest that up to the highest nominal ssDNA density used, steric hindrance and electrostatic repulsion from the bound strands do not significantly inhibit further attachment of ssDNA to the CMPs. In the following sections, we consistently report the nominal density $R(x)$ for ease of comparison, but note that $R(x)$ can be directly scaled to the experimental density using the linear relationship in Fig. 1e.

Electrophoretic mobility and hydrodynamic size of CMP–DNA conjugates exhibit a non-linear dependence on ssDNA grafting density

To characterize CMPs and CMP–DNA conjugates, we first performed agarose gel electrophoresis shift assays. All particles migrate towards the anode as a single band due to their uniform size and overall negative charge (Fig. 1f). We observed that the mobility of CMP–DNA conjugates in the gel decreases with increasing $R(x)$. To parametrize the gel shift assay, we analyzed the gel and extract relative front R_f values that indicate the migration of CMP–DNA conjugates relative to CMPs (without DNA functionalization). The R_f *vs.* $R(x)$ is well described by the Hill equation with $R_{half} = 0.42$ DNA nm^{-2} and $n = 6.3$ (Fig. 1g, the Hill equation is given in the ESI†). Here we used the Hill equation for mathematical convenience since it provides a simple expression that can fit the data and provide a measure of cooperativity *via* the Hill coefficient n. The particle hydrodynamic size D_h measured by DLS reveals a similar non-linear trend with $R(x)$ that can be described by a Hill fit with $R_{half} = 0.48$ DNA nm^{-2} and $n = 4.5$ (Fig. 1h). Our data reveal the presence of highly cooperative dynamics between the ssDNA strands on CMPs. Whereas the average number of ssDNA strands per CMP increases linearly (Fig. 1e), the hydrodynamic and electrophoretic properties of CMP–DNA conjugates change in a non-linear and cooperative manner.

Magnetic relaxation of CMPs changes cooperatively with grafting density

Next, we investigated whether the cooperative behavior of ssDNA on CMPs is reflected in the magnetic relaxation dynamics of particles. To monitor changes in the magnetization dynamics of CMPs after DNA grafting, we performed complex magnetic ac susceptibility (ACS) measurements on particle suspensions in Tris-EDTA (TE) buffer, which monitor the magnetic relaxation dynamics of particles as a function of excitation frequency. The imaginary parts of the ACS spectra of CMPs and CMP–DNA conjugates show peaks that are typical of Brownian relaxation processes (Fig. 2a).[53] The shift in the Brownian peak position toward lower frequencies indicates a slower/retarded relaxation process, corresponding to a larger hydrodynamic volume, with increasing DNA grafting density (Fig. 2a and b). The shift in the relaxation peak position matches the increasing trend in D_h measured by DLS. We found that the relaxation peak frequency f_p shifts as a function of R(x) in a non-linear manner (Fig. 2c). Similar to R_f and D_h, the dependence of the particle relaxation peak frequency f_p on $R(x)$ is well described by the Hill equation, with $R_{half} = 0.42$ DNA nm^{-2} and $n = 3.6$, again suggesting cooperative changes in the magnetic relaxation dynamics of CMPs upon ssDNA grafting.

We hypothesize that ssDNA strands go through a transition from being coiled at a low grafting density toward forming polymer brushes at a high grafting density. Notably, we found a pronounced non-linear dependence on $R(x)$ with similar R_{half} and n parameters from fitting the Hill model to the results of electrophoretic mobility, DLS, and magnetic relaxation measurements. The three analysis techniques rely on completely different working principles, but all three provide measurements of the particle size in solution.

DNA grafting increases the colloidal stability of CMPs in the presence of Mg^{2+}

To further characterize the grafted DNA shell and its response to environmental conditions, we added monovalent NaCl or divalent $MgCl_2$ salt to the TE coupling buffer and probed our CMP–DNA conjugates. For detailed characterization, we used two complementary techniques: AFM imaging of nanoparticles deposited and dried on a mica substrate (Fig. 3a–d) and DLS, which measures particles in solution. Due to the high negative charge density of DNA, both ionic strength and ion valency are expected to have significant effects on the DNA-coated nanoparticles.[54]

Under high Na^+ conditions, we found monodisperse and sparsely distributed CMPs on the mica substrate used for AFM imaging for all grafting densities (Fig. 3c, d and Fig. S1†). The particle height H from the AFM images (Fig. 3e and Fig. S3†) and the hydrodynamic diameter D_h from DLS show a consistent trend for the Na^+ conditions: the size of the particles increases with increasing grafting density, in line with the

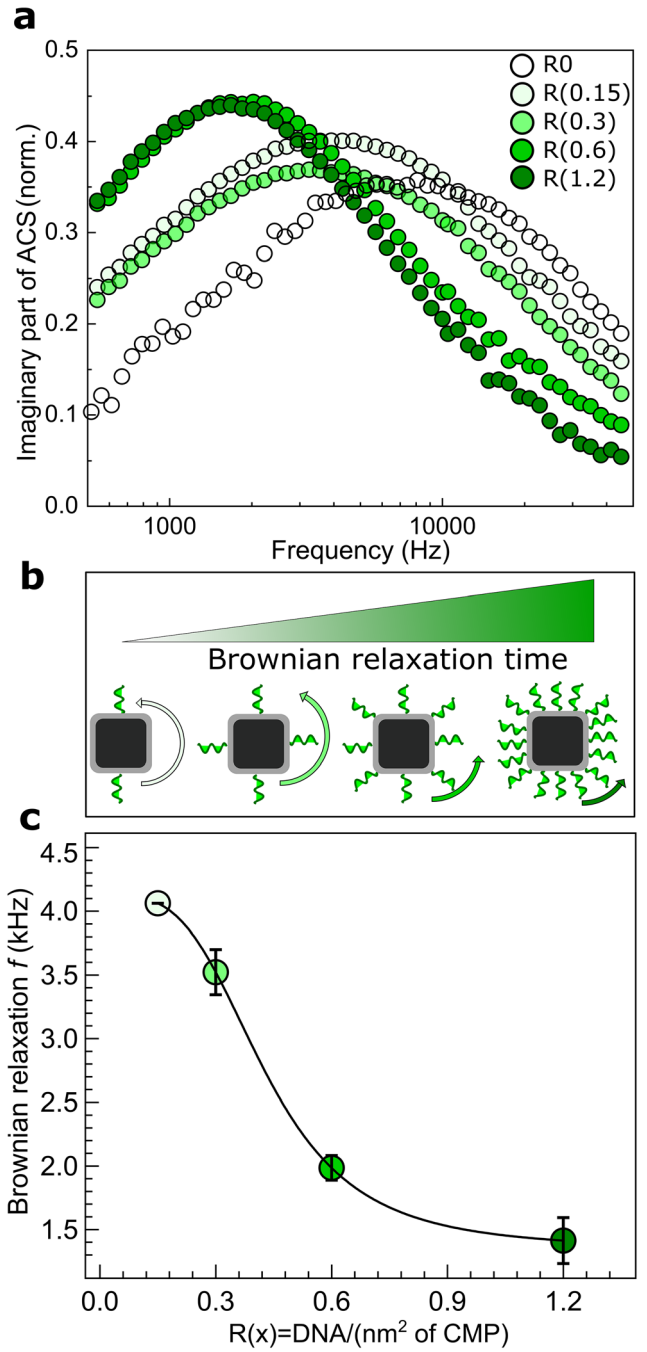

Fig. 2 Characterization of magnetic relaxation of CMPs and CMP–DNA conjugates by complex magnetic ac-susceptibility (ACS) measurements. (a) Imaginary part of the complex magnetic ac-susceptibility spectra of the $R(0)$ to $R(1.2)$ samples, showing the shift in the characteristic Brownian magnetic relaxation peak of CMPs after ssDNA grafting. (b) Schematic of the nanoparticles at different grafting densities, indicating how the particle Brownian relaxation frequency is reduced when more ssDNA strands are grafted to the CMPs. (c) Shift in the relaxation frequency f_p (mean ± SEM) after ssDNA grafting with respect to the $R(0)$ particles having no ssDNA. The ACS measurements were performed at $\mu_0 H$ = 95 μT at 22 °C on 150 μl of particle suspensions in TE buffer. The black line is a fit of the Hill model with parameters R_{half} = 0.42 DNA nm^{-2} and n = 3.6.

findings in low salt TE buffer (Fig. 1h and 3f and Fig. S4†). As expected, the D_h values from DLS are consistently larger than the heights determined by AFM under dried conditions, in agreement with a view that the DNA brushes swell in solution and that the overall solvation layer extends significantly beyond the particles' surface. This coincides also with the observation that DNA appears significantly more compact when imaged under dried conditions compared to in liquid imaging.[55]

For the Mg^{2+} conditions, AFM imaging reveals the formation of particle clusters at zero or low grafting density (Fig. 3a and 3h and Fig. S1†). Under the same conditions of high Mg^{2+} and low grafting density, the DLS data show larger average D_h than under any other conditions, again consistent with the formation of particle clusters. In the AFM images, it is possible to distinguish between individual particles and clusters. By quantifying the height of individual particles, values for H at low grafting density are very similar in the presence of Na^+ or Mg^{2+}. In contrast, by quantifying the total particle volumes including the clusters from AFM images, we found the largest average volumes for zero or low grafting density in the presence of Mg^{2+}, with values much larger than for Na^+ for the same grafting density (Fig. 3h). Altogether, these results strongly suggest that the presence of Mg^{2+} tends to induce the formation of clusters and aggregation at a low grafting density. In contrast, high grafting of ssDNA increases the colloidal stability and protects the particles against aggregation, which is desirable for many applications.

The effect of salt on the DNA shell

At a high grafting density, both the Na^+ and Mg^{2+} conditions show similar behavior. For a given high grafting density, we observed a consistent decrease in D_h going from low salt to 300 mM Na^+ and a further decrease in 5 mM Mg^{2+}, in line with the expectation that a higher salt concentration leads to a tighter less extended hydration layer and an ion atmosphere.[54] The magnitude of the changes of a few nm is similar to the change in the Debye length (which is 3–4 nm for the low salt conditions and 0.6 nm for 300 mM NaCl) and the corresponding change in the persistence length of ssDNA over this salt range.[56] However, the fact that 5 mM Mg^{2+} leads to a larger reduction in D_h than 300 mM Na^+, despite having a lower ionic strength, suggests that the divalent ions screen electrostatic interactions more efficiently than monovalent ions and lead to a tighter hydrodynamic shell.

Interestingly, for the highest grafting density, H and the particle volume decrease in the presence of Mg^{2+}, likely due to intra-strand ion bridging between ssDNA backbone charges and Mg^{2+} ions that induces compaction of ssDNA strands on the MNPs (Fig. 3g). Similar behavior has recently been shown on Au NP–DNA superstructures.[57] We derived a so-called compression-clustering propensity parameter by dividing D_h at a high salt concentration by D_h at a low/no salt concentration (Fig. 3i). In the presence of Mg^{2+}, the particles reveal a sharp transition from shell compression to particle clustering by transitioning from the high to low DNA grafting density. In

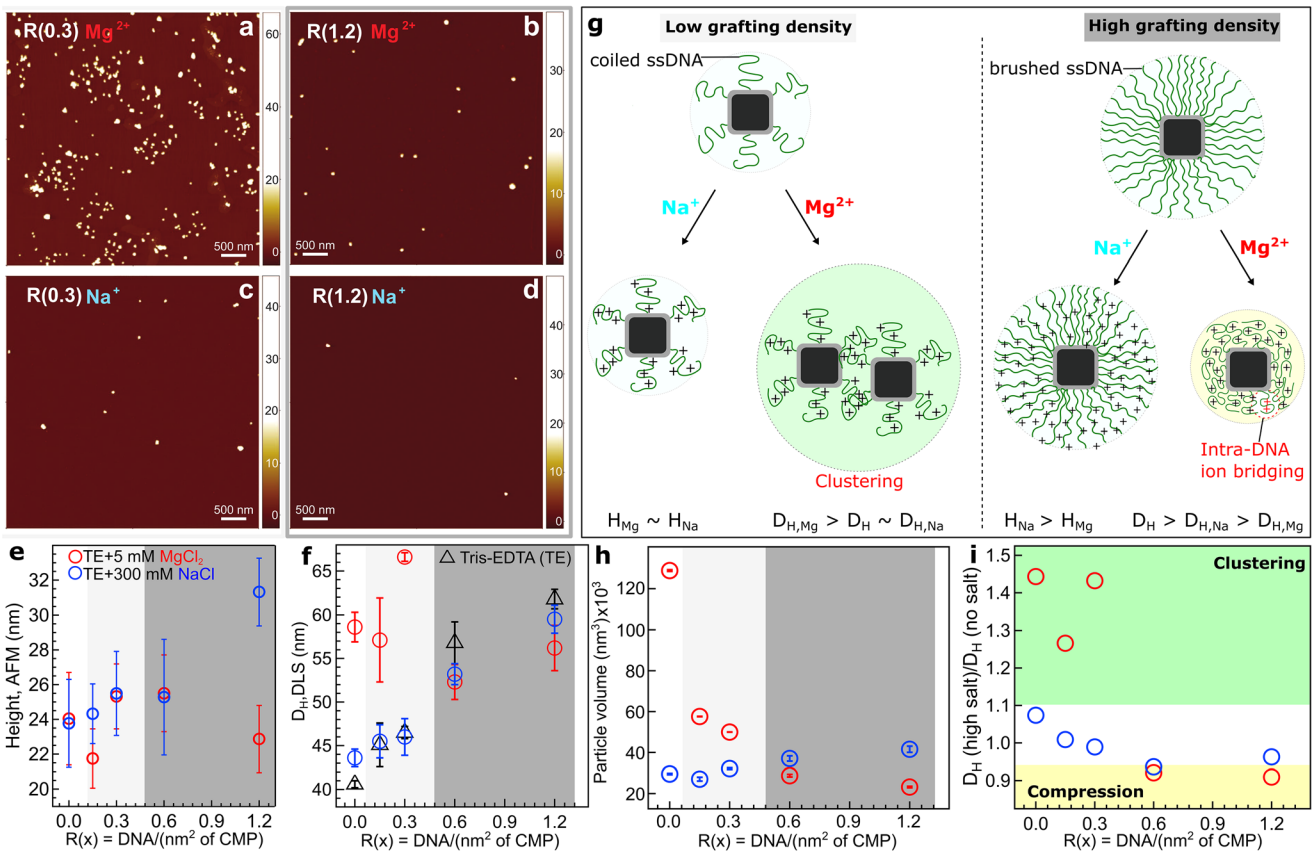

Fig. 3 Characterization of CMP–DNA conjugates by atomic force microscopy and dynamic light scattering in the presence of a monovalent or divalent salt. (a) and (c) AFM micrographs of the low ssDNA-grafted sample *R*(0.3) at 5 mM $MgCl_2$ and 300 mM NaCl concentration, respectively. (b) and (d) AFM micrographs of the high ssDNA-grafted sample *R*(1.2) under the same ionic conditions. (e) Particle heights determined from AFM as a function of *R*(*x*). The data points are the mean ± std. Only single particles are selected for analysis. (f) Volume-weighted particle hydrodynamic size D_h (mean ± SEM) of CMP–DNA conjugates *vs.* *R*(*x*) measured by DLS in TE buffer only with 5 mM $MgCl_2$ or with 300 mM NaCl. (g) Schematic illustration of CMP–DNA conjugates at low and high ssDNA grafting densities in the presence of monovalent Na^+ or divalent Mg^{2+} ions. (h) Particle volume analysis (mean ± SEM) of the AFM images. Here, clusters are also included in the analysis. (i) Ratio of D_h at a high to low/no salt concentration *vs.* *R*(*x*), revealing the compression and clustering regimes in the presence of Mg^{2+} ions. The same color code is applied to panels (e), (f), (h), and (i). The low and high grafting density regimes are highlighted with light and dark gray colors in panels (e), (f), and (h).

contrast, in the presence of Na^+, *H* and the particle volume increase further at the highest grafting density (Fig. 3e and h), suggesting that the collapse observed in Mg^{2+} is specific to divalent ions and that Na^+ appears to stabilize a dense DNA brush structure at a high grafting density. The compression-clustering parameter is close to 1 in the case of Na^+ for all grafting densities, indicating no salt-induced clustering or compression for the Na^+ conditions (Fig. 3i).

Intermediate grafting densities provide the highest sensitivity for magnetic biosensing

We next investigated whether the DNA grafting density impacts the suitability of our CMP–DNA conjugates for applications, focusing on two promising assays: magnetic-based biosensing of nucleic acids[58] and assembling on DNA origami. For magnetic biosensing, we used magnetic particle spectroscopy (MPS)[59–61] that monitors changes in the magnetic relaxation dynamics of MNPs that occur when the particle hydrodynamic size/volume increases upon hybridization of the probe DNAs on particles with the target DNA strands in solution. These changes are then reflected in the MPS higher harmonics spectrum.[62] Functionalization of CMPs with probe DNA strands and their hybridization with complementary target strands slow down the Brownian relaxation of the particles in ac magnetic fields and thereby reduce the amplitude of the MPS harmonics. The MPS higher harmonics are, however, more sensitive to changes in the particle relaxation dynamics than the fundamental excitation frequency. In particular, the 5th harmonic drops more than the 3rd harmonic upon a molecular binding event and the ratio of the 5th to 3rd harmonics (HR53) of the particles decreases upon sensing the targets compared to the HR53 of the particles without the target DNA.[63] Our magnetic assay requires no washing out or purification of unbound targets, which are critical advantages over optical lateral flow and plasmonic resonance-based schemes. They are particularly appealing for direct assays on opaque biofluids, where optical-based techniques often fail. Our CMPs with a small D_h relaxing *via* Brownian processes

(Fig. 2) are ideal for MPS-based magnetic biosensing, since small changes in the particle hydrodynamic volume can reliably be registered in the harmonics spectrum.[64]

For our biosensing assays, we labelled the CMP-DNA conjugates with a probe DNA sequence of 30 nucleotides (GC = 23.3%, T_m(25 nt) = 50.8 °C, including 5 × A as spacer) at five different grafting densities, covering a range from low to high densities (see the ESI†). To eliminate the effect of particle concentration on the assay results, we calculated the HR53 as a particle concentration-independent assay readout (see the ESI† for details).[65] We measured the change in the HR53 without (w/o) and with (w/) targets, after letting them base pair with the probe DNA on CMPs. For the sake of clarity, we present changes in the HR53 as a function of the number of the probe DNA/CMP, as determined from the depletion assays (Fig. 4a, see Fig. S5 in the ESI† for the correlation between the number of probe DNA strands and $R(x)$). The HR53 ratio shows a sigmoidal drop as a function of the probe DNA density both in the absence (Fig. 4a, black data points) and in the presence of the target strand (Fig. 4a, red data points). The relative change in the HR53 upon sensing the target reaches a maximum at the intermediate probe DNA grafting density (Fig. 4b), which tends to saturate at higher probe densities.

To cross check the assay results and show that the changes in the HR53 originate from an increase in particle hydrodynamic size, we performed DLS measurements on the same samples before and after adding the target DNA. We observed that the particle hydrodynamic size D_h increases with the probe DNA before and after adding the target DNA following a Hill function. A similar trend was observed after labeling with 20-mer thymine ($T_{(20)}$), as shown in Fig. 1. Similar to the MPS results, the relative change in D_h after sensing the target DNA reveals a maximum at the intermediate grafting density, which then drops at higher probe DNA densities (Fig. 4d). The DLS results on the particles functionalized with the 30 nt probe DNA (Fig. 4) or with 20T (Fig. 1) indicate that the cooperative dynamics of colloidal MNPs upon labeling with ssDNA is largely sequence independent for the range studied here.

We interpret the non-monotonous sensitivity to target DNA hybridization as follows: at a low grafting density, there are only relatively few DNA molecules available for binding and, therefore, the effect of DNA hybridization on particle dynamics is small (Fig. 4e). At intermediate grafting densities, near the midpoint of the Hill-like transition, we obtained a strong and reliable MPS signal change, as in this regime binding of the target DNA strongly alters particle dynamics. Finally, at the highest grafting density explored, the relative change in HR53 saturates and even decreases (Fig. 4b), likely due to the fact that densely grafted ssDNA polymer brushes on the CMPs lead to less clear changes upon hybridization (Fig. 4e). Overall, our results suggest that an intermediate grafting density is desirable for high signal-to-noise biosensing. To examine whether the hybridization efficiency and accessibility contribute to the results discussed here, we estimated the number of hybridized target DNA strands on CMPs by performing depletion assays on the supernatants collected from the assay mixture. These

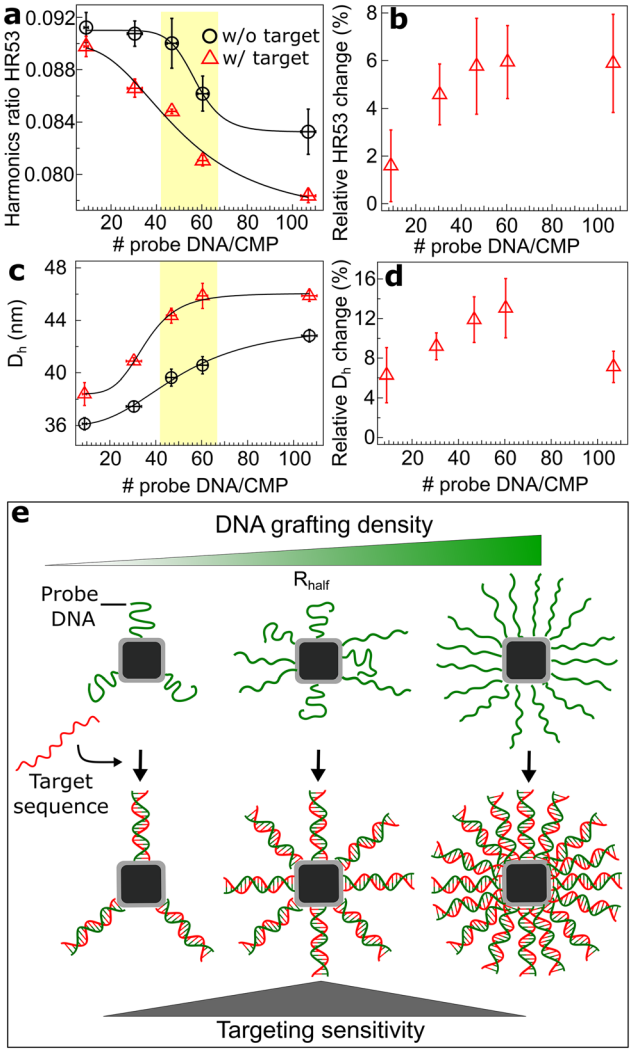

Fig. 4 Magnetic particle spectroscopy-based biosensing of target nucleic acids. (a) MPS harmonics ratio HR53 without (w/o) and with (w/) complementary target DNA at five different probe DNA grafting densities. (b) Relative change in the HR53 given by ($HR53_{probe}$–$HR53_{probe+target}$/$HR53_{probe}$) upon sensing the target DNA, which is a measure of the assay sensitivity. The MPS-based assays were performed at a typical particle concentration of 28 nM and a target DNA concentration varying from 5.2 to 29.5 μM for the lowest to highest probe DNA density, respectively, to keep the target-to-probe DNA ratio at 5. (c) Changes in the particle hydrodynamic size D_h after adding the complementary target DNA and hybridization with the probe DNA on CMPs measured by DLS. (d) Relative change in D_h upon sensing the target DNA. The data points and standard deviations in panels (a) and (c) are from three independent measurements. In panels (b) and (d), the combined uncertainties are computed according to GUM. The yellow areas in panels (a) and (c) highlight the midpoint grafting density regimes. The correlation between the number of probe DNA strands per CMP and the $R(x)$ ratio for these samples is given in detail in ESI Fig. S5 and S6.† (e) Schematic illustration of the organization of the DNA probes on CMPs depending on the grafting density. Same color coding is used in panels (a–d).

measurements revealed that the number of target *versus* probe DNA strands on CMPs can be fitted with a linear function with slope ~1 and offset ~0, showing stoichiometric binding between the target and the probe DNA on CMPs (Fig. S6†) over

the whole range. These results indicate that the hybridization efficiency plays no significant role in the results, meaning that each probe DNA will bind to a target strand under the conditions of our assay (scheme in Fig. 4e). Of note, the hybridization energy of the sequence of 25 nt targeted here is 27.8 kcal mol^{-1}, which corresponds to a dissociation constant K_d of $\sim 8.7 \times 10^{-22}$ M, implying that once duplexed, the probe and target DNA do not dissociate under the assay conditions.

High DNA grafting density favors efficient and site-specific coupling of magnetic nanoparticles to DNA origami structures

Next, we tested if the ssDNA grafting density is relevant for assembling CMP–DNA conjugates on DNA origami nanostructures. For DNA origami binding experiments, we functionalized CMPs with 20-mer thymine ($T_{(20)}$) strands and designed the DNA origami with 20-mer adenine ($A_{(20)}$) as docking sites, since this combination is a well-established and robust protocol for patterning inorganic NPs on DNA origami.[66] We prepared two different DNA origami structures: a 6 helix bundle (6HB) for dense labeling with 50 docking sites on three facets on the structure and a 24 HB for site-specific labeling with two attachment sites at opposite ends of the origami. Our DNA origami binding and agarose gel purification experiments used 11 mM Mg^{2+} to stabilize the DNA origami, even higher than the Mg^{2+} concentration of 5 mM that was observed by DLS and AFM to promote clustering at a low grafting density (Fig. 3f). We, therefore, had no success in coupling our CMP–DNA conjugates at DNA grafting densities equal or lower than the intermediate grafting density to the 6HB or 24HB DNA origami structures, mainly due to particle clustering during the binding and/or gel purification. We, however, successfully assembled our CMP–DNA conjugates at $R(x)$ = 1.2 (~110 DNA/CMP) with high efficiency on 6HB DNA origami. After separating MNP–DNA origami bundles from free DNA origami bundles by agarose gel electrophoresis, we imaged them using negative-stain TEM microscopy (Fig. 5a and c).

Analysis of the TEM images of the CMP–DNA-labelled 6HB reveals dense labeling, with on average 12.5 and up to 25 CMP–DNA conjugates per DNA origami structure (Fig. 5b, see Fig. S7† for additional TEM images). While a total of 50 docking sites for binding are available, we do not expect 50 CMPs to bind, due to steric hindrance and the fact that one nanoparticle can bind to multiple binding sites. The CMPs with the highest DNA grafting density also enable site-specific binding to 24HB structures that have two binding sites at two ends of the structure (Fig. 5c, see Fig. S8† for additional TEM images). The particle center-to-center distance determined

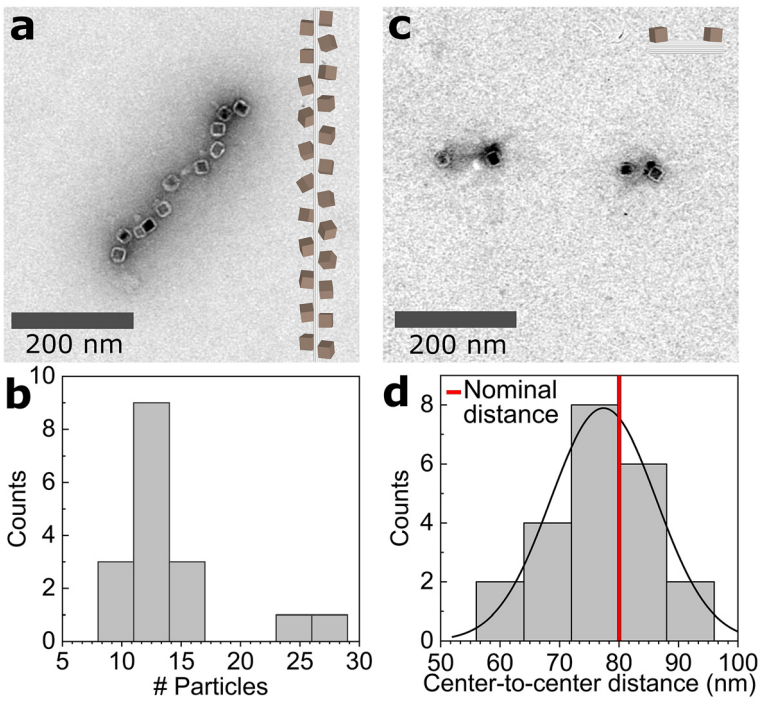

Fig. 5 Negative-stain transmission electron microscopy (TEM) analyses of the assembly of CMP–DNA conjugates on DNA origami nanostructures. (a) TEM image of the assembly of CMPs labeled with $T_{(20)}$ at a density of $R(x)$ = 1.2 to a 6HB DNA origami with ~50 $A_{(20)}$ docking sites on three facets along the structure. The inset shows a schematic of the assembly. (b) Histogram of the number of particles assembled on individual 6HB structures obtained from TEM images like the ones in panel (a) and in ESI Fig. S7.† (c) TEM image of the site-specific binding of CMP–DNA conjugates $(T)_{20}$ at $R(x)$ = 1.2 to a 24HB DNA origami with two A_{20} docking sites at two ends of the structure. (d) Histogram of particle center-to-center distance on the 24HB structures determined from TEM images like the ones shown in panel (c) and ESI Fig. S8.† The solid line is a Gaussian fit, indicating a mean particle center-to-center distance of 77.7 ± 15.8 nm (mean ± 1σ). The vertical red line is the distance between the docking sites expected from the DNA origami design.

from the TEM images obtained for gel purified structures is 77.7 ± 15.8 nm (mean ± 1σ), in good agreement with the distance of 80 nm expected from the origami design (Fig. 5d). Our results demonstrate the importance of a dense ssDNA shell around the MNPs for an effective assembly of MNPs on DNA origami nanostructures.

Conclusion

We show that our polymer encapsulated CMPs with high colloidal stability and a small particle hydrodynamic size are a powerful platform to decipher the effects of ssDNA grafting density on a range of dynamic properties of magnetic nanoparticles. We found that the magnetic relaxation, hydrodynamics, and electrophoretic mobilities change non-linearly with the number of ssDNA strands on CMPs and can be well described with the Hill equation, indicating cooperative changes. The fits of the Hill equation to gel electrophoresis mobility, dynamic light scattering, and magnetic ac-susceptibility data result in similar midpoint and rate parameters. At a low grafting density, the ssDNA strands are mainly in a coiled configuration, in contrast to the situation at a high grafting density, where the ssDNA strands form dense polymer brushes on CMPs. The brushed ssDNA strands on CMPs are compressed in the presence of divalent Mg^{2+} ions as observed in DLS and AFM analyses. We attribute this behavior to intra-DNA strand ion bridging, which is not seen in the presence of monovalent Na^{+} ions. Importantly, we found that intermediate to high DNA grafting densities enhance the colloidal stability of the CMPs and effectively prevent clustering and aggregation even in the presence of divalent ions.

Our results show that depending on the application of colloidal MNPs, different ssDNA grafting densities have to be aimed for. Using our CMP–DNA conjugates as magnetic nanomarkers for MPS-based magnetic biosensing of target nucleic acids, we found that the ssDNA probe grafting density at the midpoint of the Hill equation leads to the highest sensitivity of magnetic assays with MNPs. For coupling of CMPs to DNA origami structures, we demonstrate that high grafting densities of the ssDNA probe favor efficient and site-specific coupling. Our polymer coating protocol with clickable polymers is a versatile approach to transfer organic ligand-coated MNPs in water. By applying our polymer coating and DNA labeling approaches to MNPs that can be detected at picomolar concentrations,[49] we expect to achieve picomolar nucleic acid detection sensitivity. Our CMPs with a tunable DNA grafting density provide new opportunities, *e.g.* in combining magnetic biosensing with DNA switches such as DNA strand displacement and the development of DNA origami structures with magnetic actuation capabilities.

Author contributions

A. L. conceptualized and designed the research as an Alexander von Humboldt fellow at LMU Munich, synthesized the polymer, established polymer coating and DNA functionalization protocols, performed TEM and DLS measurements and analyses, modelled the ACS data, supervised the study, analyzed the data, and wrote the manuscript. Y. W. performed polymer coating, DNA functionalization, hybridization assays, and AGE, ACS, MPS, and DLS measurements. P. J. K. prepared AFM samples, performed measurements, and analyzed data. C. P. prepared the DNA origami, coupled particles to the DNA origami, performed negative-stain TEM imaging, and analyzed the data. M. S. C. synthesized the particles. M. C. co-developed the polymer coating procedure. F. L. and T. V. developed ACS and MPS setups. F. S., P. T., M. S., T. L., and J. T. analyzed the data. J. L. analyzed the data, supervised the study at LMU Munich, and wrote the manuscript. All authors have given approval to the final version of the manuscript.

Conflicts of interest

The authors declare no competing financial interest.

Acknowledgements

This work was supported by DFG RTG 1952 “NanoMet”, DFG LA 4923/3-1, the Junior Research Group “Metrology4life”, and the Alexander von Humboldt Foundation. J. T. was funded under DFG TA 1375/1-1 and C. P. and T. L. through the DFG SFB1032 “Nanoagents”, Project A6. We thank Margherita Gallano and Gloria Müller for the initial characterization of DNA-labelled MNPs. We thank Kerstin Frank and Petra Schmidt (TU Braunschweig) for ICP-OES measurements, Willem Vanderlinden for helpful discussions about AFM imaging, and Thomas Nicolaus for laboratory assistance.

References

1 C. A. Mirkin, R. L. Letsinger, R. C. Mucic and J. J. Storhoff, A DNA-Based Method for Rationally Assembling Nanoparticles into Macroscopic Materials*, *Nature*, 1996, **382**, 607–609, DOI: 10.4324/9780429200151-2.

2 A. P. Alivisatos, K. P. Johnsson, X. Peng, T. E. Wilson, C. J. Loweth, M. P. Bruchez Jr. and P. G. Schultz, Organization Of Nanocrystal Molecules Using DNA, *Nature*, 1996, **382**(6592), 609–611.

3 D. Nykypanchuk, M. M. Maye, D. Van Der Lelie and O. Gang, DNA-Guided Crystallization of Colloidal Nanoparticles, *Nature*, 2008, **451**(7178), 549–552, DOI: 10.1038/nature06560.

4 R. J. Macfarlane, B. Lee, M. R. Jones, N. Harris, G. C. Schatz and C. A. Mirkin, Nanoparticle Superlattice Engineering with DNA, *Science*, 2011, **334**(6053), 204–208, DOI: 10.1126/science.1210493.

5 A. G. Kanaras, Z. Wang, A. D. Bates, R. Cosstick and M. Brust, Towards Multistep Nanostructure Synthesis:

Programmed Enzymatic Self-Assembly of DNA/Gold Systems, *Angew. Chem.*, 2003, **42**, 191–194.

6 J. T. Dias, M. Moros, P. Del Pino, S. Rivera, V. Grazú and J. M. de la Fuente, DNA as a Molecular Local Thermal Probe for the Analysis of Magnetic Hyperthermia, *Angew. Chem., Int. Ed.*, 2013, **52**(44), 11526–11529, DOI: **10.1002/anie.201305835**.

7 E. L. Rösch, R. Sack, M. S. Chowdhury, F. Wolgast, M. Schilling, T. Viereck and A. Lak, Amplification and Extraction Free Quantitative Detection of Viral Nucleic Acids and Single-Base Mismatches Using Magnetic Signal Amplification Circuit, *bioRxiv*, 2022.

8 V. R. Cherkasov, E. N. Mochalova, A. V. Babenyshev, A. V. Vasilyeva, P. I. Nikitin and M. P. Nikitin, Nanoparticle Beacons: Supersensitive Smart Materials with On/Off-Switchable Affinity to Biomedical Targets, *ACS Nano*, 2020, **14**(2), 1792–1803, DOI: **10.1021/acsnano.9b07569**.

9 A. E. Prigodich, P. S. Randeria, W. E. Briley, N. J. Kim, W. L. Daniel, D. A. Giljohann and C. A. Mirkin, Multiplexed Nanoflares: MRNA Detection in Live Cells, *Anal. Chem.*, 2012, **84**(4), 2062–2066, DOI: **10.1021/ac202648w**.

10 H. Wang, R. Yang, L. Yang and W. Tan, Nucleic Acid Conjugated Nanomaterials for Enhanced Molecular Recognition, *ACS Nano*, 2009, **3**(9), 2451–2460, DOI: **10.1021/nn9006303**.

11 A. Heuer-Jungemann, R. Kirkwood, A. H. El-Sagheer, T. Brown and A. G. Kanaras, Copper-Free Click Chemistry as an Emerging Tool for the Programmed Ligation of DNA-Functionalised Gold Nanoparticles, *Nanoscale*, 2013, **5**(16), 7209–7212, DOI: **10.1039/c3nr02362a**.

12 A. F. De Fazio, A. H. El-Sagheer, J. S. Kahn, I. Nandhakumar, M. R. Burton, T. Brown, O. L. Muskens, O. Gang and A. G. Kanaras, Light-Induced Reversible DNA Ligation of Gold Nanoparticle Superlattices, *ACS Nano*, 2019, **13**(5), 5771–5777, DOI: **10.1021/acsnano.9b01294**.

13 C. Sönnichsen, B. M. Reinhard, J. Liphardt and A. P. Alivisatos, A Molecular Ruler Based on Plasmon Coupling of Single Gold and Silver Nanoparticles, *Nat. Biotechnol.*, 2005, **23**(6), 741–745, DOI: **10.1038/nbt1100**.

14 A. Kuzyk, R. Schreiber, H. Zhang, A. O. Govorov, T. Liedl and N. Liu, Reconfigurable 3D Plasmonic Metamolecules, *Nat. Mater.*, 2014, **13**(9), 862–866, DOI: **10.1038/nmat4031**.

15 A. Kuzyk, R. Schreiber, Z. Fan, G. Pardatscher, E.-M. Roller, A. Högele, F. C. Simmel, A. O. Govorov and T. Liedl, DNA-Based Self-Assembly of Chiral Plasmonic Nanostructures with Tailored Optical Response, *Nature*, 2012, **483**(7389), 311–314, DOI: **10.1038/nature10889**.

16 G. P. Acuna, M. Bucher, I. H. Stein, C. Steinhauer, A. Kuzyk, P. Holzmeister, R. Schreiber, A. Moroz, F. D. Stefani, T. Liedl, F. C. Simmel and P. Tinnefeld, Distance Dependence of Single-Fluorophore Quenching by Gold Nanoparticles Studied on DNA Origami, *ACS Nano*, 2012, **6**(4), 3189–3195, DOI: **10.1021/nn2050483**.

17 K. Trofymchuk, K. Kołątaj, V. Glembockyte, F. Zhu, G. P. Acuna, T. Liedl and P. Tinnefeld, Gold Nanorod DNA Origami Antennas for 3 Orders of Magnitude Fluorescence Enhancement in NIR, *ACS Nano*, 2023, **17**(2), 1327–1334, DOI: **10.1021/acsnano.2c09577**.

18 R. S. Mathew-Fenn, R. Das and P. A. B. Harbury, Remeasuring the Double Helix, *Science*, 2008, **322**(5900), 446–449, DOI: **10.1126/science.1158881**.

19 T. Zettl, R. S. Mathew, S. Seifert, S. Doniach, P. A. B. Harbury and J. Lipfert, Absolute Intramolecular Distance Measurements with Angstrom-Resolution Using Anomalous Small-Angle X-Ray Scattering, *Nano Lett.*, 2016, **16**(9), 5353–5357, DOI: **10.1021/acs.nanolett.6b01160**.

20 T. Zettl, R. S. Mathew, X. Shi, S. Doniach, D. Herschlag, P. A. B. Harbury and J. Lipfert, Gold Nanocrystal Labels Provide a Sequence–to–3D Structure Map in SAXS Reconstructions, *Sci. Adv.*, 2018, **4**, eaar4418, DOI: **10.1126/sciadv.aar4418**.

21 K. Hübner, M. Pilo-Pais, F. Selbach, T. Liedl, P. Tinnefeld, F. D. Stefani and G. P. Acuna, Directing Single-Molecule Emission with DNA Origami-Assembled Optical Antennas, *Nano Lett.*, 2019, **19**(9), 6629–6634, DOI: **10.1021/acs.nanolett.9b02886**.

22 B. T. Mai, S. Fernandes, P. B. Balakrishnan and T. Pellegrino, Nanosystems Based on Magnetic Nanoparticles and Thermo- or PH-Responsive Polymers: An Update and Future Perspectives, *Acc. Chem. Res.*, 2018, **51**(5), 999–1013, DOI: **10.1021/acs.accounts.7b00549**.

23 J. Lee, W. Shin, Y. Lim, J. Kim, W. R. Kim, H. Kim, J. H. Lee and J. Cheon, Non-Contact Long-Range Magnetic Stimulation of Mechanosensitive Ion Channels in Freely Moving Animals, *Nat. Mater.*, 2021, **20**(7), 1029–1036, DOI: **10.1038/s41563-020-00896-y**.

24 S. H. Chung, A. Hoffmann, S. D. Bader, C. Liu, B. Kay, L. Makowski and L. Chen, Biological Sensors Based on Brownian Relaxation of Magnetic Nanoparticles, *Appl. Phys. Lett.*, 2004, **85**(14), 2971–2973, DOI: **10.1063/1.1801687**.

25 A. Lak, M. Cassani, B. T. Mai, N. Winckelmans, D. Cabrera, E. Sadrollahi, S. Marras, H. Remmer, S. Fiorito, L. Cremades-Jimeno, F. J. Litterst, F. Ludwig, L. Manna, F. J. Teran, S. Bals and T. Pellegrino, Fe2+ Deficiencies, FeO Subdomains, and Structural Defects Favor Magnetic Hyperthermia Performance of Iron Oxide Nanocubes into Intracellular Environment, *Nano Lett.*, 2018, **18**, 6856–6866.

26 H. L. Grossman, W. R. Myers, V. J. Vreeland, R. Bruehl, M. D. Alper, C. R. Bertozzi and J. Clarke, Detection of Bacteria in Suspension by Using a Superconducting Quantum Interference Device, *Proc. Natl. Acad. Sci. U. S. A.*, 2004, **101**(1), 129–134.

27 S. J. Osterfeld, H. Yu, R. S. Gaster, S. Caramuta, L. Xu, S. J. Han, D. A. Hall, R. J. Wilson, S. Sun, R. L. White, R. W. Davis, N. Pourmand and S. X. Wang, Multiplex Protein Assays Based on Real-Time Magnetic Nanotag Sensing, *Proc. Natl. Acad. Sci. U. S. A.*, 2008, **105**(52), 20637–20640, DOI: **10.1073/pnas.0810822105**.

28 K. Wu, V. K. Chugh, V. D. Krishna, A. di Girolamo, Y. A. Wang, R. Saha, S. Liang, M. C. J. Cheeran and J. P. Wang, One-Step, Wash-Free, Nanoparticle Clustering-Based Magnetic Particle Spectroscopy Bioassay Method for

Detection of SARS-CoV-2 Spike and Nucleocapsid Proteins in the Liquid Phase, *ACS Appl. Mater. Interfaces*, 2021, **13**(37), 44136–44146, DOI: 10.1021/acsami.1c14657.

29 H. J. Chung, C. M. Castro, H. Im, H. Lee and R. Weissleder, A Magneto-DNA Nanoparticle System for Rapid Detection and Phenotyping of Bacteria, *Nat. Nanotechnol.*, 2013, **8**(5), 369–375, DOI: 10.1038/nnano.2013.70.

30 M. Strömberg, J. Göransson, K. Gunnarsson, M. Nilsson, P. Svedlindh and M. Strømme, Sensitive Molecular Diagnostics Using Volume-Amplified Magnetic Nanobeads, *Nano Lett.*, 2008, **8**(3), 816–821, DOI: 10.1021/nl072760e.

31 J. M. Perez, L. Josephson, T. O'Loughlin, D. Högemann and R. Weissleder, Magnetic Relaxation Switches Capable of Sensing Molecular Interactions, *Nat. Biotechnol.*, 2002, **20**(8), 816–820, DOI: 10.1038/nbt720.

32 J. R. Sosa-acosta, C. Iriarte-mesa, G. A. Ortega and A. M. Díaz-garcía, DNA – Iron Oxide Nanoparticles Conjugates : Functional Magnetic Nanoplatforms in Biomedical Applications, *Top. Curr. Chem.*, 2020, **378**(1), 1–29, DOI: 10.1007/s41061-019-0277-9.

33 D. B. Robinson, H. H. J. Persson, H. Zeng, G. Li, N. Pourmand, S. Sun and S. X. Wang, DNA-Functionalized MFe2O4 (M = Fe, Co, or Mn) Nanoparticles and Their Hybridization to DNA-Functionalized Surfaces, *Langmuir*, 2005, **21**(7), 3096–3103, DOI: 10.1021/la047206o.

34 F. Wang, H. Shen, J. Feng and H. Yang, PNA-Modified Magnetic Nanoparticles and Their Hybridization with Single-Stranded DNA Target : Surface Enhanced Raman Scatterings Study, *Microchim. Acta*, 2006, **153**, 15–20, DOI: 10.1007/s00604-005-0460-2.

35 R. De Palma, S. Peeters, M. J. Van Bael, H. Van Den Rul, K. Bonroy, W. Laureyn, J. Mullens, G. Borghs and G. Maes, Silane Ligand Exchange to Make Hydrophobic Superparamagnetic Nanoparticles Water-Dispersible, *Chem. Mater.*, 2007, **19**(7), 1821–1831, DOI: 10.1021/cm0628000.

36 H. H. P. Yiu, L. Bouffier, P. Boldrin, J. Long, J. B. Claridge and M. J. Rosseinsky, Comprehensive Study of DNA Binding on Iron (II,III) Oxide Nanoparticles with a Positively Charged Polyamine Three-Dimensional Coating, *Langmuir*, 2013, **29**(36), 11354–11365, DOI: 10.1021/la400848r.

37 Y. Bai, D. Roncancio, Y. Suo, Y. Shao, D. Zhang and C. Zhou, A Method Based on Amino-Modi Fi Ed Magnetic Nanoparticles to Extract DNA for PCR-Based Analysis, *Colloids Surf., B*, 2019, **179**, 87–93, DOI: 10.1016/j.colsurfb.2019.03.005.

38 K. Wagner, A. Kautz, M. Röder, M. Schwalbe, K. Pachmann, J. H. Clement and M. Schnabelrauch, Synthesis of Oligonucleotide-Functionalized Magnetic Nanoparticles and Study on Theirin Vitro Cell Uptake, *Appl. Organomet. Chem.*, 2004, **18**(10), 514–519, DOI: 10.1002/aoc.752.

39 S. Akhtar, M. Strömberg, T. Zardán Gómez de la Torre, C. Russell, K. Gunnarsson, M. Nilsson, P. Svedlindh, M. Strømme and K. Leifer, Real-Space Transmission Electron Microscopy Investigations of Attachment of Functionalized Magnetic Nanoparticles to DNA-Coils Acting as a Biosensor, *J. Phys. Chem. B*, 2010, **114**(41), 13255–13262, DOI: 10.1021/jp105756b.

40 L. Berti, T. Woldeyesus, Y. Li and K. S. Lam, Maximization of Loading and Stability of SsDNA: Iron Oxide Nanoparticle Complexes Formed through Electrostatic Interaction, *Langmuir*, 2010, **26**(23), 18293–18299, DOI: 10.1021/la103237e.

41 P. Gong, Z. Peng, Y. Wang, R. Qiao, W. Mao, H. Qian, M. Zhang, C. Li and S. Shi, Synthesis of Streptavidin-Conjugated Magnetic Nanoparticles for DNA Detection, *J. Nanopart. Res.*, 2013, **15**(4), 1558, DOI: 10.1007/s11051-013-1558-9.

42 B. Cannon, A. R. Campos, Z. Lewitz, K. a. Willets and R. Russell, Zeptomole Detection of DNA Nanoparticles by Single-Molecule Fluorescence with Magnetic Field-Directed Localization, *Anal. Biochem.*, 2012, **431**, 40–47, DOI: 10.1016/j.ab.2012.08.017.

43 Y. Guo, Y. Wang, S. Li, L. Niu, D. Wei and S. Zhang, DNA-Spheres Decorated with Magnetic Nanocomposites Based on Terminal Transfer and Cellular Targeted Drug Delivery, *Chem. Commun.*, 2017, **53**, 4826–4829, DOI: 10.1039/c7cc00310b.

44 C. Zhang, R. J. MacFarlane, K. L. Young, C. H. J. Choi, L. Hao, E. Auyeung, G. Liu, X. Zhou and C. A. Mirkin, A General Approach to DNA-Programmable Atom Equivalents, *Nat. Mater.*, 2013, **12**(8), 741–746, DOI: 10.1038/nmat3647.

45 T. A. Meyer, C. Zhang, G. Bao and Y. Ke, Programmable Assembly of Iron Oxide Nanoparticles Using DNA Origami, *Nano Lett.*, 2020, **20**, 2799–2805, DOI: 10.1021/acs.nanolett.0c00484.

46 S. Berensmeier, Magnetic Particles for the Separation and Purification of Nucleic Acids, *Appl. Microbiol. Biotechnol.*, 2006, **73**(3), 495–504, DOI: 10.1007/s00253-006-0675-0.

47 J. E. Smith, C. D. Medley, Z. Tang, D. Shangguan, C. Lofton and W. Tan, Aptamer-Conjugated Nanoparticles for the Collection and Detection of Multiple Cancer Cells, *Anal. Chem.*, 2007, **79**(8), 3075–3082, DOI: 10.1021/ac062151b.

48 K. Wu, J. Liu, R. Saha, D. Su, V. D. Krishna, M. C. J. Cheeran and J. P. Wang, Magnetic Particle Spectroscopy for Detection of Influenza A Virus Subtype H1N1, *ACS Appl. Mater. Interfaces*, 2020, **12**(12), 13686–13697, DOI: 10.1021/acsami.0c00815.

49 M. S. Chowdhury, E. L. Rösch, K. Janssen, F. Wolgast, M. Schilling, T. Viereck and A. Lak, Decoupling the Characteristics of Magnetic Nanoparticles for Ultrahigh Sensitivity, *Nano Lett.*, 2023, **23**, 58–65, DOI: 10.1021/acs.nanolett.2c03568.

50 T. Pellegrino, L. Manna, S. Kudera, T. Liedl, D. Koktysh, A. L. Rogach, S. Keller, J. Rädler, G. Natile and W. J. Parak, Hydrophobic Nanocrystals Coated with an Amphiphilic Polymer Shell: A General Route to Water Soluble Nanocrystals, *Nano Lett.*, 2004, **4**(4), 703–707, DOI: 10.1021/nl035172j.

51 Z. Jin, L. Du, C. Zhang, Y. Sugiyama, W. Wang, G. Palui, S. Wang and H. Mattoussi, Modification of Poly(Maleic

Anhydride)-Based Polymers with H2N-R Nucleophiles: Addition or Substitution Reaction?, *Bioconjugate Chem.*, 2019, **30**(3), 871–880, DOI: **10.1021/acs.bioconjchem.9b00008**.

52 W. W. Yu, E. Chang, J. C. Falkner, J. Zhang, A. M. Al-Somali, C. M. Sayes, J. Johns, R. Drezek and V. L. Colvin, Forming Biocompatible and Nonaggregated Nanocrystals in Water Using Amphiphilic Polymers, *J. Am. Chem. Soc.*, 2007, **129**(10), 2871–2879, DOI: **10.1021/ja067184n**.

53 P. C. Fannin, B. K. P. Scaife and S. W. Charles, The Measurement of the Frequency Dependent Susceptibility of Magnetic Colloids, *J. Magn. Magn. Mater.*, 1988, **72**(1), 95–108, DOI: **10.1016/0304-8853(88)90276-4**.

54 J. Lipfert, S. Doniach, R. Das and D. Herschlag, Understanding Nucleic Acid-Ion Interactions, *Annu. Rev. Biochem.*, 2014, **83**, 813–841, DOI: **10.1146/annurev-biochem-060409-092720**.

55 P. J. Kolbeck, M. Dass, I. V. Martynenko, R. J. A. Van Dijk-Moes, K. J. H. Brouwer, A. Van Blaaderen, W. Vanderlinden, T. Liedl and J. Lipfert, A DNA Origami Fiducial for Accurate 3D AFM Imaging, *Nano Lett.*, 2023, **23**(4), 1236–1243, DOI: **10.1021/acs.nanolett.2c04299**.

56 A. Y. L. Sim, J. Lipfert, D. Herschlag and S. Doniach, Salt Dependence of the Radius of Gyration and Flexibility of Single-Stranded DNA in Solution Probed by Small-Angle x-Ray Scattering, *Phys. Rev. E: Stat., Nonlinear, Soft Matter Phys.*, 2012, **86**(2), 1–5, DOI: **10.1103/PhysRevE.86.021901**.

57 S. Srivastava, A. Chhabra and O. Gang, Effect of Mono- and Multi-Valent Ionic Environments on the in-Lattice Nanoparticle-Grafted Single-Stranded DNA, *Soft Matter*, 2022, **18**(3), 526–534, DOI: **10.1039/d1sm01171e**.

58 L. Josephson, J. Manuel Perez and R. Weissleder, Magnetic Nanosensors for the Detection of Oligonucleotide Sequences, *Angew. Chem., Int. Ed.*, 2001, **40**(17), 3204–3206, DOI: **10.1002/1521-3773(20010903)40:17<3204::AID-ANIE3204>3.0.CO;2-H**.

59 X. Zhang, D. B. Reeves, I. M. Perreard, W. C. Kett, K. E. Griswold, B. Gimi and J. B. Weaver, Molecular Sensing with Magnetic Nanoparticles Using Magnetic Spectroscopy of Nanoparticle Brownian Motion, *Biosens. Bioelectron.*, 2013, **50**, 441–446, DOI: **10.1016/j.bios.2013.06.049.Molecular**.

60 H. J. Krause, N. Wolters, Y. Zhang, A. Offenhäusser, P. Miethe, M. H. F. Meyer, M. Hartmann and M. Keusgen, Magnetic Particle Detection by Frequency Mixing for Immunoassay Applications, *J. Magn. Magn. Mater.*, 2007, **311**, 436–444, DOI: **10.1016/j.jmmm.2006.10.1164**.

61 S. Draack, N. Lucht, H. Remmer, M. Martens, B. Fischer, M. Schilling, F. Ludwig and T. Viereck, Multiparametric Magnetic Particle Spectroscopy of CoFe2O4 Nanoparticles in Viscous Media, *J. Phys. Chem. C*, 2019, **123**(11), 6787–6801.

62 K. Wu, D. Su, R. Saha, D. Wong and J. P. Wang, Magnetic Particle Spectroscopy-Based Bioassays: Methods, Applications, Advances, and Future Opportunities, *J. Phys. D: Appl. Phys.*, 2019, **52**, 173001, DOI: **10.1088/1361-6463/ab03c0**.

63 A. M. Rauwerdink and J. B. Weaver, Measurement of Molecular Binding Using the Brownian Motion of Magnetic Nanoparticle Probes, *Appl. Phys. Lett.*, 2010, **96**, 033702, DOI: **10.1063/1.3291063**.

64 J. Dieckhoff, A. Lak, M. Schilling and F. Ludwig, Protein Detection with Magnetic Nanoparticles in a Rotating Magnetic Field, *J. Appl. Phys.*, 2014, **115**(2), 024701.

65 A. M. Rauwerdink and J. B. Weaver, Viscous Effects on Nanoparticle Magnetization Harmonics, *J. Magn. Magn. Mater.*, 2010, **322**(6), 609–613, DOI: **10.1016/j.jmmm.2009.10.024**.

66 T. Liedl, R. Schreiber, J. Do, E.-M. Roller, T. Zhang, V. J. Schüller, P. C. Nickels and J. Feldmann, Hierarchical Assembly of Metal Nanoparticles, Quantum Dots and Organic Dyes Using DNA Origami Scaffolds, *Nat. Nanotechnol.*, 2013, **9**(1), 74–78.